Impact of Sn substitution on the structure and magnetism of Sr_2IrO_4

Andrew F. May,[1,*] Huibo Cao,[2] and Stuart Calder[2]

[1]*Materials Science and Technology Division, Oak Ridge National Laboratory, Oak Ridge, Tennessee 37831, USA*

[2]*Neutron Scattering Division, Oak Ridge National Laboratory, Oak Ridge, Tennessee 37831, USA*

(Received 28 June 2018; published 17 September 2018)

The magnetic behavior of Sn-substituted Sr_2IrO_4 has been examined through magnetization measurements and single-crystal neutron diffraction on $Sr_2Ir_{1-x}Sn_xO_4$ for $0.05 \lesssim x \lesssim 0.35$. For all x examined, the magnetic ground state is similar to that induced in Sr_2IrO_4 by application of a magnetic field. This magnetic state is characterized by a small net moment due to the alignment of canted moments within an otherwise antiferromagnetic structure. The weak ferromagnetic behavior is observed in the magnetization data for both unique crystallographic orientations. Diffraction data reveal an anisotropic response in the lattice parameters, with an overall lattice expansion, as well as a small reduction in the rotation of the IrO_6 octahedra. The magnetic ordering temperature is continually suppressed with increasing x, and long-range magnetic order persists to the highest Sn concentrations synthesized.

DOI: 10.1103/PhysRevMaterials.2.094406

I. INTRODUCTION

Sr_2IrO_4 has become a prototype material for studying the impact of strong spin-orbit coupling on the electronic and magnetic properties of strongly correlated systems. In Sr_2IrO_4, the electronic ground state driven by Ir^{4+} has total angular momentum $J_{\text{eff}} = \frac{1}{2}$ due to crystal-field and spin-orbit effects, and the orbital moment is expected to be parallel to the spin [1]. This leads to a Mott-like insulating ground state since even a small on-site U can create a gap in the resultant ground state. The $J_{\text{eff}} = \frac{1}{2}$ state is technically realized in the limit of large spin-orbit coupling and strong (infinite) cubic crystal-field splitting, but the distortion of the octahedral environment in Sr_2IrO_4 is small enough that this model describes the main physics. The ground state of Sr_2IrO_4, with ordered magnetic pseudospin $\frac{1}{2}$ moments, is reminiscent of cuprate superconductors. Indeed, Sr_2IrO_4 is crystallographically similar to the cuprate family of high-temperature superconductors and is predicted to be a superconductor when appropriately electron-doped [2]. While La or Ga substitution for Sr yield a decrease in the electrical resistivity [3–5], consistent with electron doping, superconductivity has not been observed.

The magnetic ground state of Sr_2IrO_4 is a canted antiferromagnet with a Néel temperature of $T_N \approx 240$ K [1,6,7]. At a critical field of $H^* \approx 3$ kOe, a spin reorientation produces a weak ferromagnetic state due to alignment of canted moments within the basal plane of this tetragonal structure [1]. The net "saturation" magnetization of these canted moments is small, with less than $0.1\mu_B$/Ir observed at 2 K and 6 T [7,8]. The orientation of the moment is linked, via strong spin-orbit coupling, to the rotation of the IrO_6 octahedra [9].

Chemical substitutions have a strong influence on the magnetism in Sr_2IrO_4, in part because the $J_{\text{eff}} = \frac{1}{2}$ configuration is strongly linked to the existence of Ir^{4+} and thus any valence change disrupts the magnetism. For instance, La doping rapidly suppresses the magnetic order, causing a loss of long-range order by ≈2 at. % La (relative to Sr) [3,4]. Isoelectronic substitution of Ca for Sr leads to a relatively small change in T_N but the moment may be suppressed [10]. Substitution on the Ir site also has a dramatic impact on the magnetism, as expected. Substituting Tb for Ir leads to an incommensurate magnetic structure followed by the loss of magnetic order by only ≈3% Tb [11]. Mn substitution leads to a change in the magnetic anisotropy, with moments oriented along the c-axis for 10% substitution [12]. Ru doping leads to a similar change in magnetic anisotropy, and a collinear magnetic structure is observed up to 30% Ru [13]. In addition, a coexistence of magnetic structures has been observed for intermediate Ru concentrations, suggesting an associated electronic phase separation and a strong competition between the basal-plane and c-axis orientations of the moments [13]. The substitution of Rh for Ir also leads to a rapid decrease in T_N, with a complete loss of magnetism by ≈16% Rh [14,15]. The magnetic structure reported for modest Rh concentrations is that of the field-induced magnetic structure of Sr_2IrO_4 [15].

The general crystallographic features of Sr_2IrO_4 can be described using space group $I4_1/acd$ (No. 142), with $a = 5.4979$ Å and $c = 25.798$ Å at 300 K [6], though some finer details of the structure require a more sophisticated description [17]. Sr_2IrO_4 is the $n = 1$ compound in the Ruddlesden-Popper series $Sr_{n+1}Ir_nO_{3n+1}$, and octahedral rotations lead to supercell formation within the basal plane. A schematic of the crystal structure for Sr_2IrO_4 is shown in Fig. 1(a). The electronic behavior in this family ranges from the spin-orbit coupled Mott insulator Sr_2IrO_4 to a correlated metal for the $n = \infty$ high-pressure phase $SrIrO_3$ [18]. Interestingly, Sn substitution in $SrIrO_3$ was found to induce a metal-insulator transition concomitant with magnetic order, thus yielding a potential Slater insulator [19]. This proven ability of Sn^{4+} to substitute for Ir^{4+} and manipulate the magnetic properties motivated the current study.

*mayaf@ornl.gov

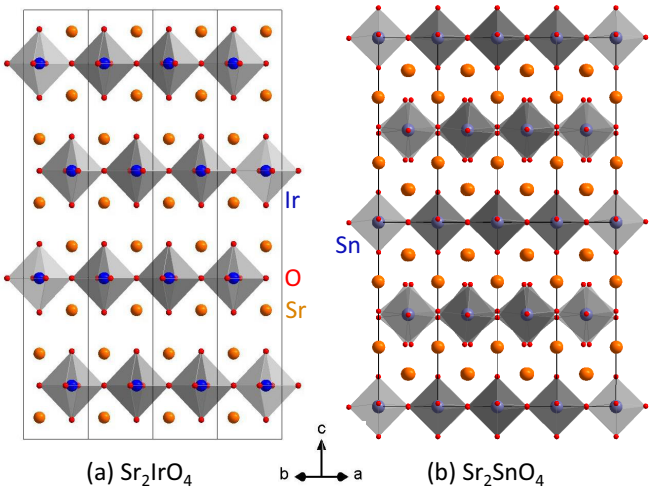

FIG. 1. Crystal structures of Sr_2IrO_4 and Sr_2SnO_4 with $(Ir,Sn)O_6$ octahedra shaded and unit cells outlined; two unit cells along c are shown for Sr_2SnO_4. Structures taken from Refs. [6,16].

Sr_2SnO_4 is a band insulator that is structurally similar to Sr_2IrO_4 [20], but it does not contain the octahedral rotations observed in Sr_2IrO_4. Rather, Sr_2SnO_4 contains octahedral tiltings, as shown in Fig. 1(b), and is described by the orthorhombic space group $Pccn$ (No. 56) up to 423 K, with room-temperature lattice parameters of $a = 5.7290$ Å, $b = 5.7352$ Å, and $c = 12.5811$ Å [16]. Above 573 K, the octahedral tiltings are lost and the K_2NiF_4 ($I4/mmm$) structure is recovered [16]. Compared to Sr_2IrO_4, Sr_2SnO_4 has an expansion of the ab plane but a contraction of the stacking distance along the c-axis; the average atomic volume in Sr_2SnO_4 is larger.

In this study, we examined the structure and magnetic behavior of $Sr_2Ir_{1-x}Sn_xO_4$ single crystals using magnetization measurements, powder x-ray diffraction, and single-crystal neutron diffraction. Sn substitution expands the lattice while contracting along the c-axis, and it leads to a small decrease in the angle of octahedral rotations. The magnetic ordering temperature T_N decreases with increasing x, and long-range magnetic order remains at the highest Sn concentration examined ($x \approx \frac{1}{3}$). All Sn-containing crystals possess a zero-field ground state that differs from that in Sr_2IrO_4, and this spin structure is similar to the field-induced magnetic state of Sr_2IrO_4. One notable difference is that the "weak ferromagnetic" behavior in $Sr_2Ir_{1-x}Sn_xO_4$ is observed for both crystallographic orientations, suggesting enhanced ferromagnetic character that may be associated with canting of the moments along the c-axis.

II. EXPERIMENTAL DETAILS

Details of the crystal growth are provided in Sec. III A. Phase purity and the evolution of the lattice parameters were examined using powder x-ray diffraction with data collected on a PANalytical X'Pert Pro MPD using monochromated Cu $K_{\alpha,1}$ radiation. Many crystals were pulverized to obtain these diffraction patterns. Rietveld refinements and Le Bail fittings were performed using FULLPROF [21].

Single-crystal neutron diffraction measurements were performed at the High Flux Isotope Reactor (HFIR) at Oak Ridge National Laboratory (ORNL). Diffraction data utilized to obtain the nuclear structure were collected on the Four Circle Diffractometer (HB-3A) at $T = 295$ K using a wavelength of 1.003 Å. All crystal structure refinements were performed within the space group $I4_1/acd$ (No. 142) using FULLPROF [21]. The small moment of Ir^{4+} combined with its ability to absorb neutrons makes characterization of the magnetic scattering challenging. As such, the fixed-incident energy triple-axis spectrometer (HB-1A) at HFIR was utilized to examine the magnetic behavior of $Sr_2Ir_{1-x}Sn_xO_4$ crystals at $T = 5$ K using a wavelength of 2.36 Å. The crystals were oriented in the $(H0L)$ scattering plane, with scattering in the $(0KL)$ equivalent due to the neutron beam illuminating the full sample and therefore measuring all domains. HB-1A offers excellent signal to background ratio due to the analyzer after the sample, the highly oriented PG filters, and the double bounce monochromator design, and it has been used before to study magnetism in Sr_2IrO_4 [12,13,22]. The crystals utilized were selected from growths with nominal compositions of $x = 0.05$ and 0.30.

Energy-dispersive spectroscopy (EDS) was performed in a Hitachi TM3000 scanning electron microscope using a tungsten filament and a Bruker Quantax detector. The reported values for x in $Sr_2Ir_{1-x}Sn_xO_4$ were obtained from the resulting atomic percents assuming full site occupancy as $x_{EDS} = \frac{\%Sn}{\%Sn+\%Ir}$. Average values and standard deviations for x_{EDS} of individual crystals are reported, and x_{nom} refers to the nominal melt composition for a given growth.

A Quantum Design Magnetic Property Measurement System was utilized to measure the magnetization M as a function of temperature and applied field H. Magnetic transition temperatures T_N were calculated by a linear extrapolation of M^2 versus T below T_N to a linear background obtained just above T_N. Due to the small induced magnetization above T_N, this procedure is similar to extrapolating the M^2 versus T to $M^2 = 0$. T_N values were obtained using data collected upon cooling in an applied field of 100 Oe oriented perpendicular to the c-axis (the orientation with the largest induced moment).

III. RESULTS AND DISCUSSION

A. Crystal growth and chemical homogeneity

For crystal growth, we initially followed the method described by Sung *et al.* and obtained crystals that were 1–2 mm in dimension [8]. We then optimized the growth process for our conditions, obtaining Sr_2IrO_4 crystals with dimensions of 4 mm or larger in some cases. Magnetization and electrical resistivity measurements on our Sr_2IrO_4 crystals were reported in Ref. [23] and were found to be consistent with high-quality Sr_2IrO_4 on the basis of the data reported by Sung *et al.* Single crystals were grown from a $SrCl_2$ flux using mixtures of molar concentrations $7SrCl_2$, $2SrCO_3$, $(1-x)IrO_2$, and $xSnO_2$. Our optimized growth process involved heating to 1000 °C and dwelling for 4 h, heating at 60°/h to 1300 °C and then cooling to 900 °C at 5°/h. The growths occurred in a Pt crucible with a Pt lid that was bent tightly around the edges, and batch sizes of ≈10 g total mass were typical. Upon Sn substitution,

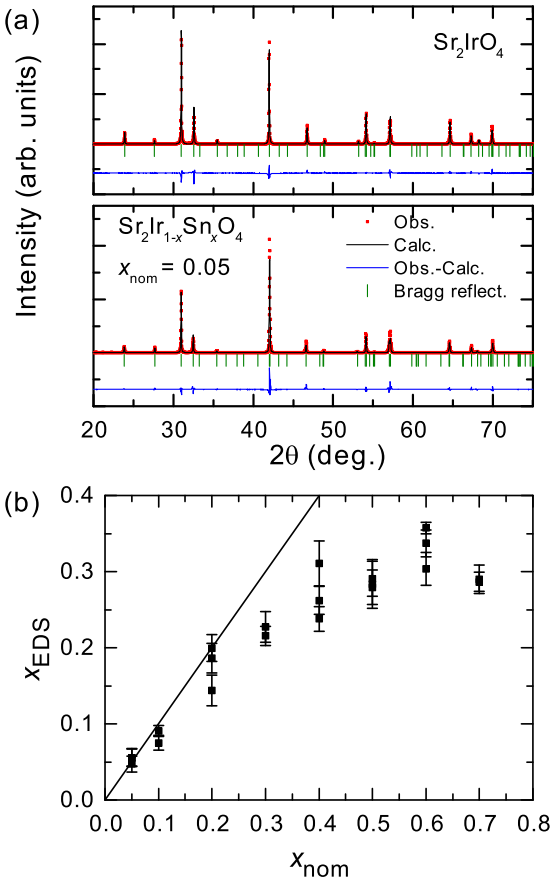

FIG. 2. (a) Powder x-ray diffraction data for ground crystals of (upper) Sr_2IrO_4 and (lower) $Sr_2Ir_{0.95}Sn_{0.05}O_4$. Rietveld refinements and difference patterns are also shown along with ticks marking the location of Bragg peaks. (b) Energy-dispersive spectroscopy (EDS) results for chemical composition as a function of nominal melt composition; error bars are standard deviations, and the solid line represents $x_{EDS} = x_{nom}$.

the size of the single crystals decreased notably, dropping to a maximum dimension of approximately 2 mm at $x_{nom} = 0.05$. However, crystals suitable for anisotropic magnetization measurements and single-crystal neutron diffraction were obtained for large x_{nom}.

Chemical homogeneity was examined, on a macroscopic scale, by performing x-ray diffraction on powders obtained by grinding many crystals. Data and Rietveld refinements for Sr_2IrO_4 and $x_{nom} = 0.05$ [$x_{EDS} = 0.05(1)$] are shown in Fig. 2(a). Diffraction experiments were complemented by EDS analysis of two to three crystals per growth, with several spots examined on each crystal. As observed in Fig. 2(b), the results suggest that the Sn content of our crystals is limited near $x_{EDS} \approx \frac{1}{3}$. For $x_{nom} = 0.05$ we observe $x_{EDS} = 0.05(1)$, but for all other growths x_{EDS} is lower than x_{nom}. The magnetic ordering temperature generally decreased with increasing x_{nom}, despite the nonoptimized growth conditions, indicating that small changes in x are likely important as the Sn content approaches the percolation threshold of 40.7% [24]. Greater inhomogeneity within a batch was observed in the range $0.2 \leqslant x_{nom} \leqslant 0.4$. Chemical phase separation was not observed within the resolution limit of our SEM ($\approx 1\ \mu$m).

For $x_{nom} \leqslant 0.1$, the powder diffraction data revealed only the Sr_2IrO_4 phase, with some peak broadening that potentially relates to stacking faults. Growths with $x_{nom} \geqslant 0.5$ also possessed a well-defined Sr_2IrO_4 phase that contained broadened peaks, and the secondary phase $SrSnO_3$ was clearly detected by x-ray diffraction of the (ground) products. The products at intermediate Sn concentrations ($0.2 \leqslant x_{nom} \leqslant 0.4$) were not homogeneous, most notably for $x = 0.2$ and 0.3. As noted, this yielded a larger spread in the observed x_{EDS} and thus x_{EDS} was obtained for the individual crystals for which magnetization data are reported. For these growths, refinement of the powder diffraction data requires two $Sr_2Ir_{1-x}Sn_xO_4$ phases to account for the splitting of Bragg peaks that is observable at large 2θ. However, additional broadening is also present and the refinements are of lower quality than for the other regions of x_{nom} that were investigated. These data reveal that growth at different Sn concentrations occurred during the crystallization process for $0.2 \leqslant x_{nom} \leqslant 0.4$. This is not necessarily limited to inhomogeneity between crystals, but it may exist across one crystal given the two-dimensional growth of these platelike crystals. This does not suggest a region of immiscibility, because the relative expansion of the lattice appears to be continuous. Such macroscopic inhomogeneity can occur when the distribution coefficient (relative solubility in liquid to solid phases) changes during growth, for instance as a function of T or as a function of composition (evaporative losses). Thus, these results are likely related to the particular synthetic conditions. Optimizing the growth conditions based on Sr_2SnO_4 would likely result in crystals with higher Sn concentrations and perhaps greater homogeneity. Such an effort was beyond the scope of this initial investigation of $Sr_2Ir_{1-x}Sn_xO_4$.

B. Structural evolution

The lattice response to Sn substitution is anisotropic, with a expanding and c contracting as x increases. This trend is shown in Fig. 3, where results from Le Bail fitting of powder x-ray diffraction data are plotted as a function of Sn content. These results are complemented by refinements of single-crystal neutron diffraction data that allow a high-quality structural refinement because neutron diffraction is strongly sensitive to the position of oxygen atoms. In general, the structural changes observed are consistent with what one would expect based on the crystal structures and local bonding environments in Sr_2IrO_4 and Sr_2SnO_4.

Sn substitution causes an overall expansion of the lattice [Fig. 3(b)], which is consistent with the larger size of Sn^{4+} compared to Ir^{4+} [25]. However, it may be useful to verify the valence of Sn through future measurements to prove that this idea of an isovalent substitution is correct. The lattice changes follow Vegard's law reasonably well (dashed lines in Fig. 1), and thus the lattice parameters can potentially be utilized to estimate the composition provided that the symmetry does not change upon further substitution. The magnetic properties may be more sensitive to both the average and local compositions.

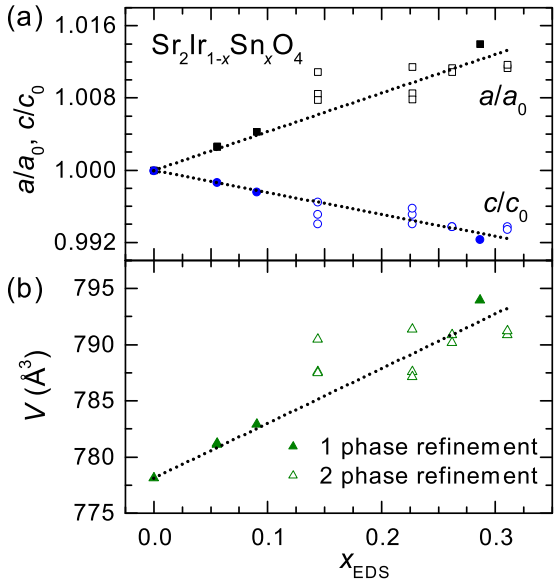

FIG. 3. Evolution of the lattice with Sn substitution obtained from Le Bail fitting: (a) lattice parameters normalized to those of Sr_2IrO_4 and (b) unit cell volume. Closed markers represent results from refinements where only one $Sr_2Ir_{1-x}Sn_xO_4$ phase was utilized. Open markers are for results where two unique $Sr_2Ir_{1-x}Sn_xO_4$ phases were refined and the results are of lower reliability, including an expectation of greater uncertainty for x_{EDS}. The dashed line shows Vegard's law adjusted for the symmetry difference by using an average in-plane lattice parameter for $x = 1$ as well as the change in stacking along the c-axis. The relative errors in x_{EDS} can be inferred from Fig. 2(b), and the errors from the Le Bail fitting for the lattice parameters are smaller than the data markers.

Single-crystal neutron diffraction was measured from crystals of $x_{nom} = 0.05$ and 0.30, and the refined compositions were $Sr_2Ir_{0.92(4)}Sn_{0.08(4)}O_4$ and $Sr_2Ir_{0.74(5)}Sn_{0.26(5)}O_4$. The $x = 0.30$ growth resulted in obvious chemical inhomogeneity in the bulk powder x-ray diffraction data obtained by grinding several crystals. However, we did not observe unusual peak shapes or splitting in our wide-angle data collected on HB-3A at HFIR, suggesting a primary domain with a reasonably homogeneous composition was measured.

Refinement of the single-crystal diffraction data revealed the change in the local bonding induced by Sn substitution, and pertinent results are in Table I. Figure 4 is provided to aid in understanding the reported bond distances and the nature of the octahedral rotation. The (Ir, Sn)O_6 octahedra expand with increasing x and the Sr-O apical bond (along c-axis) contracts. While Sn substitution enlarges the octahedra, their tetrahedral distortion (apical/basal IrO_6) does not vary much with Sn content. This may be coupled with the reduction in octahedral rotations upon increasing x. The tetrahedral distortion of octahedra and their angle of rotation are thought to be especially important for determining the magnetic ground state in Sr_2IrO_4 due to large spin-orbit coupling combined with extended orbitals [26].

While these phases can be viewed as layered materials, the crystal structure is clearly three-dimensional. The shortest Sr-O bond is along the c-axis, and a strengthening of this apical bond is likely the reason that c contracts while ab expands upon Sn substitution. In a simple picture, Sn substitution expands the lattice and pushes the basal plane Sr-O bonds further apart. This allows the apical Sr-O bond distance to be reduced, providing the contraction along the c-axis that is observed experimentally.

TABLE I. Summary of bond distances from refinements of single-crystal neutron diffraction data ($T = 295$ K), with refined compositions provided and distances in Å. The ratio of apical to basal bonds represents the tetrahedral distortion "c/a" for the (Ir, Sn)O_6 octahedra. The angle of octahedral rotations α is also provided, and $\alpha = 11.05(5)$ in Sr_2IrO_4 [6].

	$Sr_2Ir_{0.92(4)}Sn_{0.08(4)}O_4$	$Sr_2Ir_{0.74(5)}Sn_{0.26(5)}O_4$
apical Sr-O	2.4748(9)	2.4643(7)
basal Sr-O	2.7527(4)	2.7696(4)
apical IrO_6	2.0610(8)	2.0648(5)
basal IrO_6	1.9790(7)	1.9855(5)
apical/basal IrO_6	1.0414(5)	1.0399(4)
α (deg.)	10.8(2)	9.9(1)

C. Magnetic characterization

Magnetization M measurements revealed a qualitative change in the ground-state magnetism upon Sn substitution, as well as a continuous decrease of the magnetic ordering temperature T_N with increasing x. In Fig. 5, we focus on a comparison of the data for Sr_2IrO_4 and $x_{EDS} = 0.05(1)$. After establishing the qualitative change upon Sn doping, the trends observed with increasing Sn content are discussed.

Sr_2IrO_4 is a canted antiferromagnet with moments lying in the basal plane. Experimentally, this results in a cusp in $M(T)$ just below the Néel temperature of $T_N = 240$ K for small applied fields [Fig. 5(a)] [8]. When the applied field is within the basal plane and greater than $H^* \approx 3$ kOe, M follows a ferromagnetic-like increase with decreasing temperature. This behavior is associated with a spin reorientation that leads to an uncompensated moment due to the alignment of canted moments. For $H \| c$, the cusplike shape of $M(T)$ is maintained and the induced moment decreases with decreasing T below T_N. The anisotropy and metamagnetic transition can be observed in the isothermal magnetization data shown in Fig. 5(b). The anisotropy observed in the ordered state

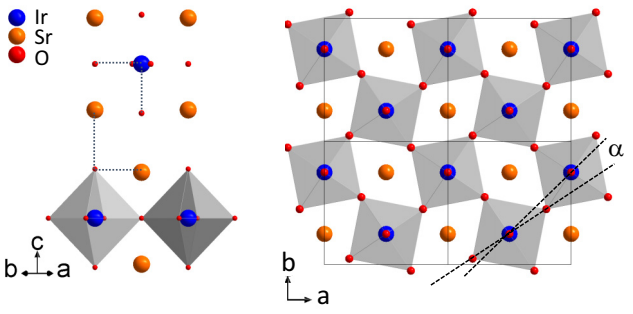

FIG. 4. Schematic to demonstrate crystallographic details of Sr_2IrO_4, with the angle of octahedral rotation α defined, and the dashed lines in the image on the left are related to the bond distances in Table I.

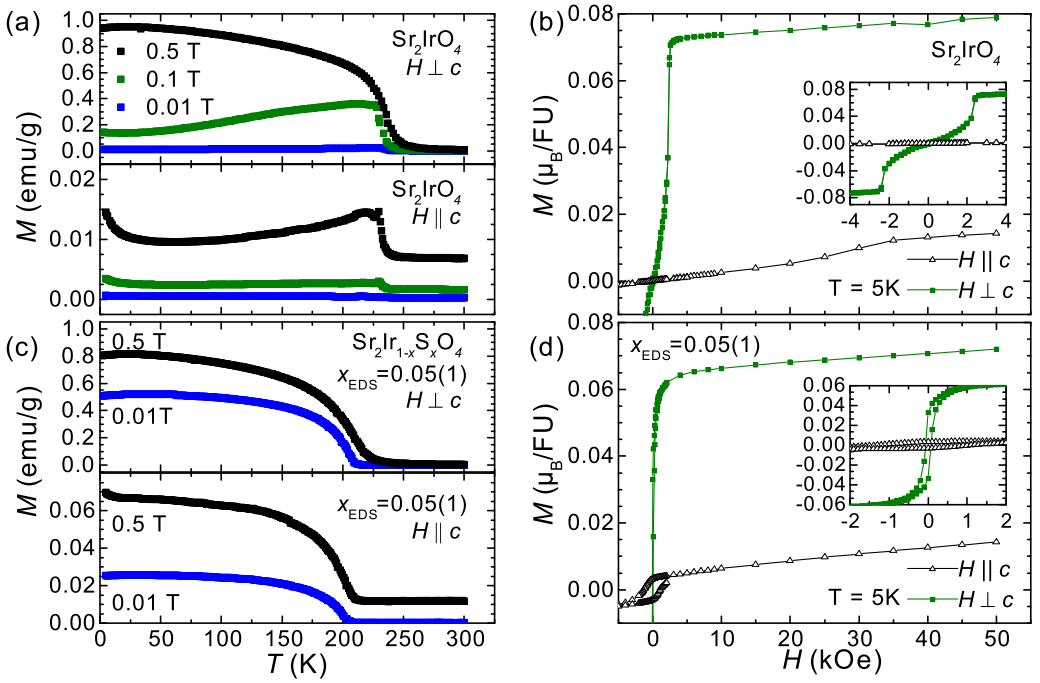

FIG. 5. Comparison of the anisotropic magnetization data for Sr_2IrO_4 and $Sr_2Ir_{0.95(1)}Sn_{0.05(1)}O_4$ single crystals. Temperature-dependent curves are shown in (a), (c), and parts (b), (d) plot the isothermal magnetization data with insets that emphasize data near $H = 0$ with units that are the same as those of the main panels. The data in (b), (d) were collected upon decreasing the magnetic field.

of Sr_2IrO_4 is also observed in the paramagnetic state near room temperature. For $H \| c$, the induced moment is nearly independent of T while M decreases with increasing T for $H \perp c$ in the region 250–300 K.

The temperature-dependent magnetization data in Fig. 5(c) demonstrate that even minor Sn substitution [$x_{EDS} = 0.05(1)$] causes a change in the ground state. In this case, $M(T)$ has a ferromagnetic-like behavior for all applied fields investigated, and this behavior is observed regardless of the orientation of the applied field. The change in magnetic character upon Sn substitution can also be observed in the isothermal magnetization curves shown in Fig. 5(d). The Sn-containing crystal has an $M(H)$ curve that looks very much like a ferromagnet with easy-plane anisotropy. A small remanence and coercivity exist, with the coercivity largest for $H \| c$ while the remanence is greatest for $H \perp c$. In this sense, $Sr_2Ir_{1-x}Sn_xO_4$ may be considered a weak ferromagnet, but the induced moment is small, and neutron diffraction shows the system is best described as a canted antiferromagnet with some net polarization.

As shown in Fig. 6(a), the magnetic ordering temperature decreases with increasing x. The extracted T_N values are plotted versus x_{EDS} in Fig. 6(b). For the largest x, the magnetization data suggest that the crystals are inhomogeneous [$M(T)$ does not increase smoothly below T_N]. Powder diffraction data suggest that large x_{nom} results in one dominant x value for a given crystal growth, and thus these results suggest that the magnetism is very sensitive to x near $x = 0.3$. This may suggest that the critical composition is being approached, in which case one would expect a deviation from the linear decrease in T_N with x that is observed for $x < 0.25$.

To minimize the effects of inhomogeneity, small crystals were selected for magnetization measurements. For $x = 0.05$, we used a 5.7 mg crystal for the magnetization measurements, in comparison to data for $x = 0$ being reported for an 11.6 mg crystal. For $x \geqslant 0.1$, the crystals utilized weighed between 1.3 and 2.2 mg. Due to the small moment on Ir^{4+}, crystals of this mass have a small signal in the measurement of the

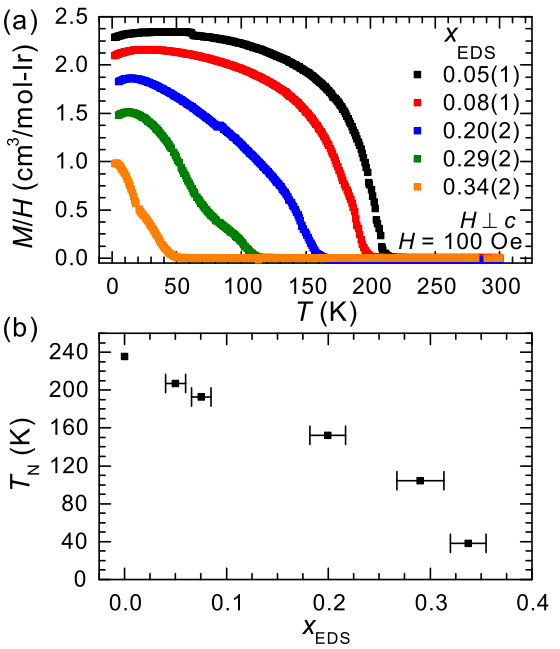

FIG. 6. (a) Temperature-dependent magnetization for different Sn concentrations in $Sr_2Ir_{1-x}Sn_xO_4$ with x_{EDS} provided in the legend. (b) Magnetic ordering temperatures extracted from the $M(T)$ data. Data were obtained upon cooling in a field applied perpendicular to the c-axis.

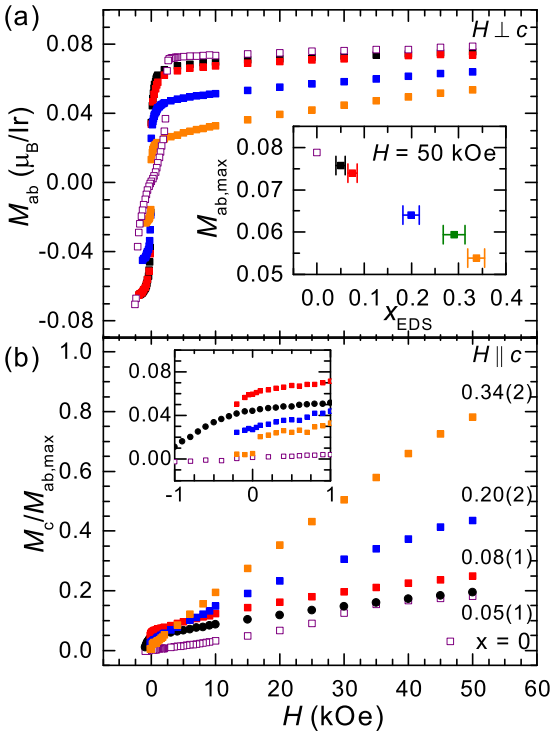

FIG. 7. Isothermal magnetization data at $T = 5$ K as a function of Sn content as indicated by x_{EDS} values in panel (b). (a) In-plane magnetization data with an inset showing the maximum induced moment obtained for each sample at $H = 50$ kOe. Data were obtained upon decreasing the field, and a remanent moment exists in each Sn-containing sample. (b) Anisotropy in the induced moment demonstrated using a normalization of the $H \| c$ moment M_c, with the inset showing data near $H = 0$ in the same units as the main panel.

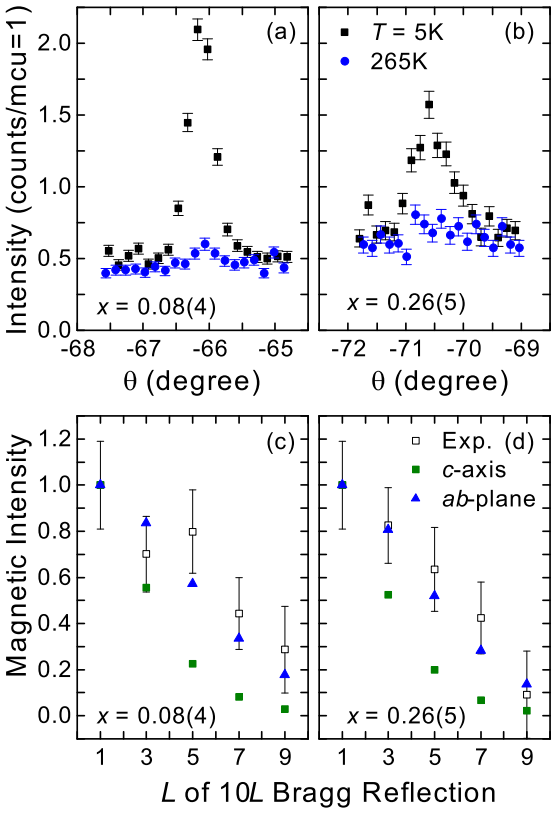

FIG. 8. Single-crystal neutron diffraction data with samples identified by refined x values. (a), (b) Comparison of neutron diffraction intensities at the 103 Bragg reflection for $T = 265$ and 5 K. The difference between these is taken as the magnetic contribution, and (c), (d) plot the integrated magnetic intensity of $10L$ reflections as a function of L. Model calculations for the magnetic structures assuming either ab plane or c-axis oriented moments are shown as closed markers in comparison to the data.

induced magnetization. In addition, we focused on low-field measurements to accurately characterize T_N in this system that possesses a ferromagnetic-like $M(T)$. This effect of low moments is amplified by the anisotropy in M that is observed in Sr_2IrO_4 above T_N, with fairly similar behavior observed in the Sn-substituted samples. The negligible temperature dependence for M above T_N when $H \| c$ leads to what looks like the onset of magnetization (moments) together with the onset of magnetic order. However, due to the presence of some temperature dependence for $H \perp c$ at large x above T_N, and the difficulty in accurately measuring such small magnetic signals, we do not think that the local moment of Ir^{4+} has been lost in the high-temperature state for large x. Future measurements to probe this behavior would likely require the production of large, polycrystalline samples that would allow the response of the high-T state to be more accurately probed.

The isothermal magnetization data at $T = 5$ K are shown for various x values in Fig. 7. The inset of Fig. 7(a) plots the "maximum" magnetization $M_{ab,max}$ as a function of x_{EDS}, where $M_{ab,max}$ is obtained at $H = 50$ kOe for $H \perp c$. In Fig. 7(b), the induced moment for $H \| c$ (M_c) is normalized to the corresponding $M_{ab,max}$. The purpose of this plot is to reveal the evolution of the magnetic anisotropy with increasing x. At high fields, the induced moment along the c-axis increases with increasing x, and thus this demonstrates a reduction in the anisotropy energy with increased Sn content. The low-field data are somewhat different. At $H = 0$, after decreasing the magnetic field, the remanent moment is largest for $x_{EDS} = 0.08(1)$ while for $x_{EDS} = 0.34(2)$ the remanence is nearly zero.

The magnetic ground state was characterized with neutron scattering to access the microscopic arrangement of the Ir moments. Magnetic scattering was measured using the Triple Axis Spectrometer HB1A at HFIR because a low background is required when searching for small magnetic signals. A measurement at 265 K provided the baseline for nuclear contributions to the Bragg reflections. We observed relatively strong magnetic scattering at $10L$ Bragg reflections for $L =$ odd at $T = 5$ K, as observed in Figs. 8(a) and 8(b), where rocking curves above and below the magnetic ordering temperatures are shown for the 103 Bragg reflection. The magnetic scattering at $10L$ ($L =$ odd) Bragg reflections can possess contributions from moments projected both parallel and perpendicular to the c-axis. These results are clearly different from those for Sr_2IrO_4, where magnetic scattering is observed at $10L$ for $L =$ even. We note that a weak intensity at $10L$ for $L =$ even was detected from the crystal with a refined composition of $Sr_2Ir_{0.92(4)}Sn_{0.08(4)}O_4$, but this was not observed for the $Sr_2Ir_{0.74(5)}Sn_{0.26(5)}O_4$ crystal. This "extra"

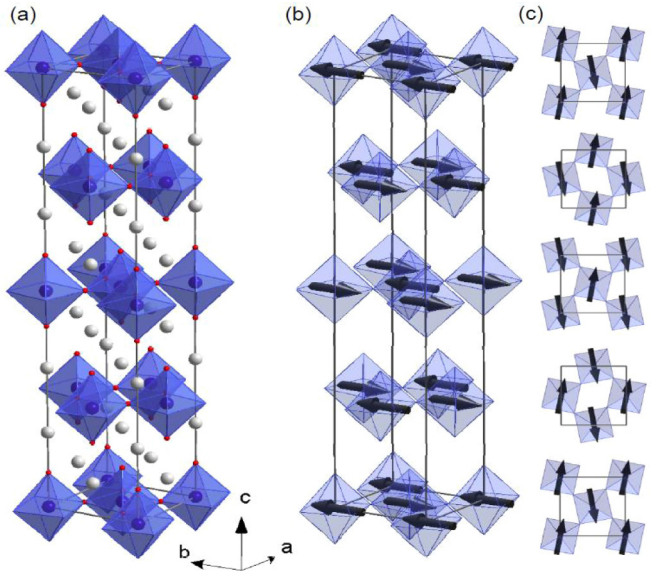

FIG. 9. (a) Crystal structure and (b) schematic of the refined magnetic structure for $Sr_2Ir_{1-x}Sn_xO_4$ with only octahedra and magnetic moments shown. (c) Perspective of each $(Ir,Sn)O_6$ layer as viewed along the c-axis.

scattering for the $Sr_2Ir_{0.92(4)}Sn_{0.08(4)}O_4$ crystal was excluded from analysis, and may have been caused by inhomogeneity of the Sn/Ir sublattice or a competition of magnetic phases that is beyond the resolution of our data.

Given the weak nature of magnetic scattering in Sr_2IrO_4 and $Sr_2Ir_{1-x}Sn_xO_4$ crystals, an unconstrained fit to determine the orientation of the moments is not necessarily reliable. As such, magnetic scattering from neutron diffraction data for Sr_2IrO_4 is typically analyzed by comparing constrained models (in-plane versus out-of-plane moments) [12,13,22,27]. To allow contributions to the moments to be both in the ab plane and along the c axis would require a combination of two irreducible representations, and the data do not offer enough reflections to sufficiently constrain this more complicated model; corrections for absorption and instrumental resolution are also required. The analysis is further complicated in Sr_2IrO_4-based crystals where $10L$ (L = odd) reflections possess a nuclear contribution. A discussion of the symmetry considerations for these magnetic structures is presented in Refs. [12] and [22].

In Figs. 8(c) and 8(d) the magnetic scattering intensity is fit to models with either ab-plane or c-axis oriented moments. For both crystals, the fit utilizing ab-plane moments provides the better characterization of the data, but this does not exclude the possibility of some small contribution from a projection of the moment onto the c-axis. Thus, the refined magnetic structure shown in Fig. 9 is the same as that proposed for the field-induced spin structure of Sr_2IrO_4, though we again emphasize that some projection of the moment along the c-axis is possible. For this magnetic structure, we refined moments of $0.20(5)\mu_B$/Ir for a refined $x = 0.08(4)$, and $0.16(5)\mu_B$/Ir for a refined $x = 0.26(5)$. These results are compared to refined moment of $0.203(3)\mu_B$/Ir reported for Sr_2IrO_4 at $T = 4$ K [22].

IV. DISCUSSION AND SUMMARY

The results above clearly indicate that a small concentration of Sn in Sr_2IrO_4 leads to an abrupt change of the zero-field magnetic ground state. At the lowest Sn concentration examined, $x \approx 0.05$, the magnetic order is qualitatively similar to that obtained in Sr_2IrO_4 in the field-induced state. The most significant difference seems to be in the magnetic anisotropy. The net moment is mostly in the basal plane, as in Sr_2IrO_4, but Sn substitution is found to enhance the moment induced along the c-axis (even at $H = 0$). Thus, this suggests that Sn induces (or enhances) a canting of the moment out of the ab plane. The neutron diffraction data could not be used to examine this in greater detail, but these data do not rule out the possibility of some moment along the c-axis. Finally, a small remanence and coercivity are observed (extrinsic effects), potentially making the term "weak ferromagnet" even more applicable than in the case of undoped Sr_2IrO_4. With increasing x, the magnetic anisotropy weakens further, perhaps suggesting a decrease in the spin orbit interaction as Sn expands the lattice and moves the systems toward the limit of a band insulator.

The data revealed a decrease in the induced magnetization with increasing x (Fig. 7), which could have multiple causes. One source would be a decrease in the Ir^{4+} moment with increasing Sn concentration. The neutron diffraction data are perhaps consistent with this, as the refined moment corresponding to $x = 0.26(5)$ was found to be $0.16(5)\mu_B$/Ir (79% of that in Sr_2IrO_4). Measurements of the susceptibility in large polycrystalline samples would aid in this discussion, as these results would reveal if the material obeys the Curie-Weiss law with an effective moment that trends with x. Another source could be an increased fraction of fluctuating moments caused by the suppression of T_N, and this would impact the ordered moment obtained by refinements of neutron diffraction data. A more exotic explanation might be the delocalization of the Ir moment among the entire octahedra. However, the expansion of the lattice (octahedra) might be anticipated to enhance the localization of the moment. This effect of expansion may contribute to the persistence of long-range order for $x \approx \frac{1}{3}$. Thus, magnetic dilution and the corresponding decrease in T_N seem to be the most likely cause for the apparent decrease in the ordered/induced moment with increasing x.

In comparison to the affects of other dopants on Sr_2IrO_4, Sn substitution induces behavior most similar to that of Rh substitution. Most notably, both Sn and Rh doping induce magnetic structures that are similar to the field-induced state of Sr_2IrO_4 [15]. Similar to Sn substitution, Rh substitution changes the magnetic anisotropy, with an increase in the moment that is induced when $H \| c$ [14]. The Rh-doped samples do not display coercivity and remanence, as observed here. The lattice response is not the same for these two substitutions. Sn substitution leads to a net expansion despite a contraction along the c-axis, while Rh substitution leads to a contraction along all unit cell directions [14]. Both substitutions lead to a slight decrease in the angle of the octahedral rotations [14,15].

Rh substitution leads to a loss of magnetic order by about 16%, while magnetic order persists in $Sr_2Ir_{1-x}Sn_xO_4$ until at least $x = 0.3$. The difference may be associated with the

net quantity of defects induced. Clancy *et al.* utilized x-ray absorption spectroscopy to determine the valence state of the Rh atoms, and found Rh to be in the Rh^{3+} state as opposed to Rh^{4+} (Rh is directly above Ir in the Periodic Table). This implies a doubling of the magnetic dilution for each Rh dopant due to the associated formation of Ir^{5+}. As such, it may be best to compare $2x$ of Rh-doped samples to the x value of isovalent substitutional elements such as Sn.

Electronically, Rh substitution results in hole doping that leads to lower resistivity [14,15]. This could also have a destabilizing effect on the magnetism, such as for the case of electron doping by La [3]. Our preliminary resistance measurements (not shown) suggest that Sn substitution leads to an increase in the resistivity. The characterization of the insulating state has been of great interest to understand if Sr_2IrO_4 may be a Slater insulator. Haskel *et al.* examined the influence of pressure on Sr_2IrO_4, and found that 17 GPa suppressed the magnetism while the insulating state remained at 40 GPa [28]. Also, Ir vacancies have been shown to increase the resistivity while decreasing T_N. These results show that magnetic order and the insulating state can be isolated from one another, suggesting that a Mott insulating description is more appropriate than the Slater picture [29].

Fine structural details are expected to have an impact on the magnetism in Sr_2IrO_4 [26,30]. For instance, Liu *et al.* examined the impact of octahedral rotations and the tetrahedral distortion on the magnetic ground state [26]. They predict a change in the ground state from the observed ab-plane canted antiferromagnet to an ab-plane collinear antiferromagnet for octahedral rotations $\alpha < 4^\circ$ (experimentally $\alpha \approx 11^\circ$ for Sr_2IrO_4). In $Sr_2Ir_{1-x}Sn_xO_4$, we observed $\alpha \approx 10^\circ$ and thus the effect of reduced octahedral rotations in $Sr_2Ir_{1-x}Sn_xO_4$ might be rather small. Similarly, the observed change in the tetrahedral distortion appears to be negligible with respect to the calculations of Liu *et al.* However, the net expansion is rather substantial and this likely plays an important role. To the best of our knowledge, only La substitution provides a similar lattice response, both in anisotropy and in total volume. For the $Sr_{1-x}La_xIrO_4$ system, this lattice response has been attributed to electron-doping that occurs with increasing x [3]. These structural changes aside, one clear difference with Sn substitution is that Sn should act as a magnetic vacancy due to its filled $4d$ electron shell. This magnetic dilution likely drives the decrease in T_N. Thus, Sn substitution in Sr_2IrO_4 appears to be unique in that it provides magnetic dilution and anisotropic lattice expansion via an isoelectronic substitution. It is interesting, though, that for even $x = 0.05$ these magnetic vacancies lead to a ground state with a net polarization and not simply a weakened magnetic state. One appropriate comparison to make is with Zn substitution in the cuprates, such as in $La_2Cu_{1-x}Zn_xO_4$ [31]. In both systems, these nonmagnetic species (Zn^{2+}, Sn^{4+}) should not induce carrier doping and thus act to add magnetic vacancies that suppress the antiferromagnetic T_N. In $La_2Cu_{1-x}Zn_xO_4$, though, T_N is suppressed to near zero by $x = 0.10$, well below the percolation limit of $x = 0.41$. In $Sr_2Ir_{1-x}Sn_xO_4$, long-range magnetic order persists to relatively large x and may indeed have a critical concentration near $x = 0.4$. This implies that Sn doping is either stabilizing the magnetism, perhaps via lattice expansion, or that Zn doping in the cuprates is more complex than simple magnetic dilution.

Strong spin-orbit coupling links the orientation of the moment to that of the IrO_6 octahedra in Sr_2IrO_4. From this perspective, the existence of a c-axis component of the moment in $Sr_2Ir_{1-x}Sn_xO_4$ could be caused by a slight octahedral tilting. Octahedral tiltings are prominent in the low-to-moderate temperature phases of Sr_2SnO_4 [16] and thus such tiltings may also occur in $Sr_2Ir_{1-x}Sn_xO_4$. For small x, such tiltings may be incoherent across the crystal, but one could speculate that the application of a magnetic field could produce coherence that results in a net moment along c. This may explain the $M_c(H)$ behavior observed near $H = 0$ for $x_{EDS} \lesssim 0.2$ in Fig. 7(b). Further structural studies would be necessary to examine this in detail.

In summary, we have shown that Sn substitution causes a change in the magnetic ground state in Sr_2IrO_4, which is best described as a canted antiferromagnet with a net moment. This result adds to a body of experimental data that demonstrate Sr_2IrO_4 can be readily modified to access competing magnetic ground states. Together with the literature, this research suggests that theoretical calculations of magnetic ground states that are both non-collinear and noncompensated should be considered when examining the available phase space for Sr_2IrO_4.

ACKNOWLEDGMENTS

This work was supported by the U.S. Department of Energy, Office of Science, Basic Energy Sciences, Materials Sciences and Engineering Division. This research used resources at the High Flux Isotope Reactor, a DOE Office of Science User Facility operated by the Oak Ridge National Laboratory. We thank Paula Lampen-Kelley for assistance with preliminary electrical measurements, and we gratefully acknowledge J. Yan and M. A. McGuire for useful discussions. We also acknowledge W. Tien for support during the HB-1A measurements.

This manuscript has been authored by UT-Battelle, LLC under Contract No. DE-AC05-00OR22725 with the U.S. Department of Energy. The U.S. Government retains and the publisher, by accepting the article for publication, acknowledges that the U.S. Government retains a nonexclusive, paid-up, irrevocable, worldwide license to publish or reproduce the published form of this manuscript, or allow others to do so, for U.S. Government purposes. The Department of Energy will provide public access to these results of federally sponsored research in accordance with the DOE Public Access Plan (http://energy.gov/downloads/doe-public-access-plan).

[1] B. J. Kim, H. Ohsumi, T. Komesu, S. Sakai, T. Morita, H. Takagi, and T. Arima, Science **323**, 1329 (2009).

[2] H. Watanabe, T. Shirakawa, and S. Yunoki, Phys. Rev. Lett. **110**, 027002 (2013).

[3] X. Chen, T. Hogan, D. Walkup, W. Zhou, M. Pokharel, M. Yao, W. Tian, T. Z. Ward, Y. Zhao, D. Parshall, C. Opeil, J. W. Lynn, V. Madhavan, and S. D. Wilson, Phys. Rev. B **92**, 075125 (2015).

[4] K. Horigane, M. Fujii, H. Okabe, K. Kobayashi, R. Horie, H. Ishii, Y. F. Liao, Y. Kubozono, A. Koda, R. Kadono, and J. Akimitsu, Phys. Rev. B **97**, 064425 (2018).

[5] T. Han, Y. Wang, J. Yang, L. He, J. Xu, D. Liang, H. Han, M. Ge, C. Y. Xi, W. K. Z. C. Zhang, and Y. Zhang, Appl. Phys. Lett. **109**, 192409 (2016).

[6] M. K. Crawford, M. A. Subramanian, R. L. Harlow, J. A. Fernandez-Baca, Z. R. Wang, and D. C. Johnston, Phys. Rev. B **49**, 9198 (1994).

[7] S. Chikara, O. Korneta, W. P. Crummett, L. E. DeLong, P. Schlottmann, and G. Cao, Phys. Rev. B **80**, 140407 (2009).

[8] N. H. Sung, H. Gretarsson, D. Proepper, J. Porras, M. L. Tacon, A. V. Boris, B. Keimer, and B. J. Kim, Philos. Mag. **96**, 413 (2016).

[9] S. Boseggia, H. C. Walker, J. Vale, R. Springell, Z. Feng, R. S. Perry, M. M. Sala, H. M. Rønnow, S. P. Collins, and D. F. McMorrow, J. Phys.: Condens. Matter **25**, 422202 (2013).

[10] G. Zhou, X. Gu, X. Yang, X. Gao, K. Wang, J. Peng, F. Zhang, and X. S. Wu, AIP Adv. **7**, 055823 (2017).

[11] J. C. Wang, S. Aswartham, F. Ye, J. Terzic, H. Zheng, D. Haskel, S. Chikara, Y. Choi, P. Schlottmann, R. Custelcean, S. J. Yuan, and G. Cao, Phys. Rev. B **92**, 214411 (2015).

[12] S. Calder, G.-X. Cao, M. D. Lumsden, J. W. Kim, Z. Gai, B. C. Sales, D. Mandrus, and A. D. Christianson, Phys. Rev. B **86**, 220403 (2012).

[13] S. Calder, J. W. Kim, G.-X. Cao, C. Cantoni, A. F. May, H. B. Cao, A. A. Aczel, M. Matsuda, Y. Choi, D. Haskel, B. C. Sales, D. Mandrus, M. D. Lumsden, and A. D. Christianson, Phys. Rev. B **92**, 165128 (2015).

[14] T. F. Qi, O. B. Korneta, L. Li, K. Butrouna, V. S. Cao, X. Wan, P. Schlottmann, R. K. Kaul, and G. Cao, Phys. Rev. B **86**, 125105 (2012).

[15] J. P. Clancy, A. Lupascu, H. Gretarsson, Z. Islam, Y. F. Hu, D. Casa, C. S. Nelson, S. C. LaMarra, G. Cao, and Y.-J. Kim, Phys. Rev. B **89**, 054409 (2014).

[16] W. T. Fu, D. Visser, K. S. Knight, and D. J. W. Ijdo, J. Solid State Chem. **177**, 4081 (2004).

[17] D. H. Torchinsky, H. Chu, L. Zhao, N. B. Perkins, Y. Sizyuk, T. Qi, G. Cao, and D. Hsieh, Phys. Rev. Lett. **114**, 096404 (2015).

[18] S. J. Moon, H. Jin, K. W. Kim, W. S. Choi, Y. S. Lee, J. Yu, G. Cao, A. Sumi, H. Funakubo, C. Bernhard, and T. W. Noh, Phys. Rev. Lett. **101**, 226402 (2008).

[19] Q. Cui, J.-G. Cheng, W. Fan, A. E. Taylor, S. Calder, M. A. McGuire, J.-Q. Yan, D. Meyers, X. Li, Y. Q. Cai, Y. Y. Jiao, Y. Choi, D. Haskel, H. Gotou, Y. Uwatoko, J. Chakhalian, A. D. Christianson, S. Yunoki, J. B. Goodenough, and J.-S. Zhou, Phys. Rev. Lett. **117**, 176603 (2016).

[20] B. Prijamboedi, S. Umar, and F. Failamani, *Shock Compression of Condensed Matter - 2015: Proceedings of the Conference of the American Physical Society Topical Group on Shock Compression of Condensed Matter*, AIP Conf. Proc. No. 1656 (AIP, New York, 2015), p. 030001.

[21] J. Rodríguez-Carvajal, Physica B **192**, 55 (1993).

[22] F. Ye, S. Chi, B. C. Chakoumakos, J. A. Fernandez-Baca, T. Qi, and G. Cao, Phys. Rev. B **87**, 140406 (2013).

[23] E. J. Moon, A. F. May, P. Shafer, E. Arenholz, and S. J. May, Phys. Rev. B **95**, 155135 (2017).

[24] M. E. J. Newman and R. M. Ziff, Phys. Rev. Lett. **85**, 4104 (2000).

[25] R. D. Shannon, Acta Cryst. A **32**, 751 (1976).

[26] P. Liu, S. Khmelevskyi, B. Kim, M. Marsman, D. Li, X.-Q. Chen, D. D. Sarma, G. Kresse, and C. Franchini, Phys. Rev. B **92**, 054428 (2015).

[27] C. Dhital, T. Hogan, Z. Yamani, C. de la Cruz, X. Chen, S. Khadka, Z. Ren, and S. D. Wilson, Phys. Rev. B **87**, 144405 (2013).

[28] D. Haskel, G. Fabbris, M. Zhernenkov, P. P. Kong, C. Q. Jin, G. Cao, and M. van Veenendaal, Phys. Rev. Lett. **109**, 027204 (2012).

[29] X. Z. Yu, N. Kanazawa, Y. Onose, K. Kimoto, W. Z. Zhang, S. Ishiwata, Y. Matsui, and Y. Tokura, Nat. Mater. **10**, 106 (2011).

[30] G. Jackeli and G. Khaliullin, Phys. Rev. Lett. **102**, 017205 (2009).

[31] R. Lichti, C. Boekema, J. Lam, D. Cooke, S. Cox, S. Ting, and J. Crow, Physica C **180**, 358 (1991).